AGU PUBLICATIONS

JGR

Journal of Geophysical Research: Space Physics

RESEARCH ARTICLE

10.1002/2014JA019882

Simulation of magnetic cloud erosion during propagation

W. B. Manchester IV[1], J. U. Kozyra[1], S. T. Lepri[1], and B. Lavraud[2,3]

[1]Department of Atmospheric Oceanic and Space Sciences, University of Michigan, Ann Arbor, Michigan, USA, [2]Institut de Recherche en Astrophysique et Planétologie, Université de Toulouse , Toulouse, France, [3]Centre National de la Recherche Scientifique, UMR 5277, Toulouse, France

This article is a companion to *Kozyra et al.* [2014], doi:10.1002/2013JA019748.

Key Points:
- Filament material can move to the front of ICMEs
- Flux rope erosion can occur by azimuthal transport of poloidal flux

Correspondence to:
W. B. Manchester IV,
chipm@umich.edu

Citation:
Manchester, W. B., IV, J. U. Kozyra, S. T. Lepri, and B. Lavraud (2014), Simulation of magnetic cloud erosion during propagation, *J. Geophys. Res. Space Physics*, *119*, 5449–5464, doi:10.1002/2014JA019882.

Received 11 FEB 2014
Accepted 30 MAY 2014
Accepted article online 3 JUN 2014
Published online 9 JUL 2014

Abstract We examine a three-dimensional (3-D) numerical magnetohydrodynamic (MHD) simulation describing a very fast interplanetary coronal mass ejection (ICME) propagating from the solar corona to 1 AU. In conjunction with its high speed, the ICME evolves in ways that give it a unique appearance at 1 AU that does not resemble a typical ICME. First, as the ICME decelerates far from the Sun in the solar wind, filament material at the back of the flux rope pushes its way forward through the flux rope. Second, diverging nonradial flows in front of the filament transport poloidal flux of the rope to the sides of the ICME. Third, the magnetic flux rope reconnects with the interplanetary magnetic field (IMF). As a consequence of these processes, the flux rope partially unravels and appears to evolve to an entirely unbalanced configuration. At the same time, filament material at the base of the flux rope moves forward and comes in direct contact with the shocked plasma in the CME sheath. We find evidence that such remarkable behavior has actually occurred when we examine a very fast CME that erupted from the Sun on 2005 January 20. In situ observations of this event near 1 AU show very dense cold material impacting the Earth following immediately behind the CME sheath. Charge state analysis shows this dense plasma is filament material. Consistent with the simulation, we find the poloidal flux (B_z) to be entirely unbalanced, giving the appearance that the flux rope has eroded. The dense solar filament material and unbalanced positive IMF B_z produced a number of anomalous features in a moderate magnetic storm already underway, which are described in a companion paper by Kozyra et al. (2014).

1. Introduction

Coronal mass ejections (CMEs) are large-scale expulsions of plasma and magnetic flux from the solar corona into the heliosphere. The ejected magnetic field is believed for many reasons to have the topology of a flux rope, which forms in a filament channel either prior to or during the CME eruption [*Low*, 2001]. A filament channel is characterized by photospheric magnetic fields that reverse radial direction at a well-defined polarity inversion line (PIL), while the horizontal field runs nearly parallel to the PIL. Here is where filaments form as cold dense concentrations of plasma suspended in the corona at chromospheric temperatures with densities 100 times greater than the surrounding corona. Filaments are found embedded in low density cavities, which are themselves surrounded by the dense plasma of the streamer belt. As a CME erupts, a flux rope is expelled from the corona with much of the three-part structure intact [*Hundhausen*, 1993; *Gibson and Low*, 1998]. The bright core composed of filament material is found at the back (sunward side) of the flux rope, the plasma cavity is at the front of the rope, while the dense plasma of the surrounding streamer leads the flux rope.

The ejected material from CMEs is routinely observed at 1 AU where plasma properties and magnetic field are measured in situ. Here the interplanetary CME (ICME) is often in the configuration of a magnetic cloud, which is characterized by high field strengths and smooth field rotations indicative of a magnetic flux rope [*Burlaga et al.*, 1981, 1982, 1987]. Careful examination may allow this interplanetary flux rope to be directly connected to the rope ejected from the corona [*Démoulin*, 2008]. However, connecting the components of the CME three-part density structure to in situ counterparts is often not possible. While a pileup of plasma is commonly found ahead of the flux rope, signatures of a cavity within the flux rope are not as clear. ICME expansion tends to produce densities (and kinetic temperatures) lower than that of the surrounding solar wind, but there are often density fluctuations within the cloud that attain or exceed the ambient value [*Burlaga et al.*, 1981, 1982], which may obscure the signatures of the cavity.

The core/filament material can best be identified in situ by ion charge states, which offer a key to distinguishing different structures within a CME that are determined by the ionization environment before the eruption. Heavy ion charge states such as He^{+}, C^{2-3+}, O^{2-4+}, and Fe^{4-6+} are the dominant constituents of CME filament material as shown by observations made with SOHO/UVCS (Ultraviolet Coronagraph Spectrometer) [see *Lee and Raymond*, 2012, and references therein]. In the absence of heating, these ionization states become frozen into the solar wind as the density decreases and collisions become negligible by 4 R_s [*Hundhausen et al.*, 1968; *Ko et al.*, 1999]. Hence, the presence of cold filament material may be clearly distinguished by its frozen-in ionization states in interplanetary space [*Schwenn et al.*, 1980; *Burlaga et al.*, 1998; *Skoug et al.*, 1999; *Yao et al.*, 2010; *Sharma and Srivastava*, 2012].

An example of in situ identification of low charge state filament material is presented by *Gopalswamy et al.* [1998] who examined the 7–11 February 1997 CME/ICME event. They noted dense filament material in SOHO/LASCO (Large Angle and Spectrometric Coronagraph) C2 coronagraph images lagging behind the front of the CME, and corresponding cold dense filament material was found at the back of a magnetic cloud found by Wind to be populated with relatively high abundances of Fe^{5+} and Fe^{6+}. However, such convincing in situ charge state evidence of filament material has been rarely found. A review of 10 years of data from (Solar Wind Ion Composition Spectrometer) SWICS/ACE [*Lepri and Zurbuchen*, 2010] found only 11 events (4% of those surveyed) with low ionization charge states that were indicative of filament material. This apparent conflict may have been resolved by *Lee and Raymond* [2012] who found that low-ionization filament material (as observed by UVCS) covers only a few percent of the total area of CMEs, which is consistent with the low rate of in situ detection.

As an ICME propagates through the heliosphere, there are many complex ways in which it can interact with the solar wind that may deform and disguise the flux rope ejected from the Sun. As the solar wind approaches a constant radial velocity, the aspect ratio of the ICME flux rope will increase [*Riley et al.*, 2004], while the bimodal wind tends to bend the flux rope into an outward-concave shape [*Riley et al.*, 2004; *Manchester et al.*, 2004b]. Fast moving CMEs will drive shocks and accrete plasma from the solar wind [*Manchester et al.*, 2004a; *Lugaz et al.*, 2005]. While the flux rope may maintain its overall structure to 1 AU, it may also reconnect with the interplanetary magnetic field (IMF), which will erode the flux rope and produce an imbalance in the poloidal flux (the twist component of the rope's field, which will be the z component assuming the axis of the rope is near the Earth's orbital plane). Examples of flux rope erosion include the 21 January 2005 ICME, which has a large imbalance in B_z that has been attributed to magnetic reconnection by *Dasso et al.* [2006]. Similarly, *Ruffenach et al.* [2012] and *Lavraud et al.* [2014] closely examined several CME events and found evidence (including reconnection jets) that magnetic reconnection occurred on the front side of the flux rope leading to its erosion. Magnetic clouds were studied with many spacecraft including STEREO A, B, ACE, Wind, and Time History of Events and Macroscale Interactions during Substorms.

In this paper, we consider how the density structure of an ICME, specifically the filament material, may evolve to affect the magnetic field in a way that would suggest that significant reconnection has occurred. We begin by examining the simulation of *Manchester et al.* [2006], which modeled the CME component of the Carrington Event. This severe space weather event encompasses a sequence of phenomena that began with a white-light flare observed on 1 September 1859 that was subsequently followed by a severe geomagnetic storm 17 h and 40 min later. The CME simulation we consider was designed to attain this short Sun-to-Earth transit time and provide a model of the conditions at Earth that were taken as input for a magnetospheric simulation of the resulting geomagnetic storm [*Ridley et al.*, 2006]. While not the original subject of paper, the simulation provides us an opportunity to examine how an extremely fast ICME may evolve from Sun to Earth. The model CME is driven by a three-dimensional magnetic flux rope imbedded with a canonical three-part density structure. With an initial speed of approximately 4000 km/s, the CME undergoes strong deceleration as it propagates in the solar wind, which is consistent with observations [*Jones et al.*, 2007]. We will show that momentum of the dense filament material leads to its forward movement through the decelerating flux rope, which in turn drives flows that displace the poloidal field leading to a localized region of unbalanced flux at the nose of the rope. Such flux imbalances have previously been interpreted to be the result of magnetic reconnection [*Dasso et al.*, 2006].

In relationship to this model, we examine the 20 January 2005 CME that erupted from the Sun at very high speed ($\approx$ 3000 km/s). The extreme speed of this CME is similar to the Carrington Event and provides the

basis for comparison with the simulation of *Manchester et al.* [2006]. In the case of the 20 January 2005 CME, the associated ICME arrived at Earth with a number of very unusual features. First, the fact that the ICME magnetic field is highly imbalanced suggests that it may have undergone extensive reconnection with the IMF [*Dasso et al.*, 2006]. Second, very dense plasma in the ICME was in an unexpected location, being found immediately following the sheath rather than being at the sunward side of the ICME ejecta as expected from the CME's observed three-part structure. These two specific features are consistent with the simulation of *Manchester et al.* [2006], and the physical processes by which the forward movement of filament material within the ejecta displaces the poloidal field resulting in unbalanced flux.

The geomagnetic storm that resulted on 21 and 22 January is also anomalous. It was moderate by measure of minimum *Dst* but in other ways behaved more like a superstorm. A brief equatorial super-fountain and strong ion-atom aurora appeared. Until now, both have been observed almost exclusively during superstorms [cf., *Basu et al.*, 2001; *Tsurutani et al.*, 2004; *Zhang et al.*, 2006]. The filament material was captured into the magnetosphere to form a cold dense plasma sheet (CDPS) with associated magnetotail stretching, its high dynamic pressure amplified Joule heating rates in the cusp region, and the CDPS (formed of captured filament material) acted as a high-density plasma source to intensify the ring current during northward IMF conditions. A rich variety of geospace phenomena, linked to the presence of the solar filament material, are described in an overview paper [*Kozyra et al.*, 2013] and the companion paper [*Kozyra et al.*, 2014], which provides more details of the event.

The organization of the paper is as follows: We first give a brief summary of the model of *Manchester et al.* [2006] in sections 2 and 3. In section 4, we completely reevaluate the simulation with a focus on the evolution of the ICME magnetic field and the filament material, and in section 5, we compare the model to the 20 January 2005 event. Finally, in section 6, we summarize our findings and point out the direction for future work.

2. Governing Equations of the MHD Model

The numerical simulation of *Manchester et al.* [2006] describes the corona and heliosphere as a magnetized fluid that behaves thermodynamically as an ideal gas with a polytropic index, $\gamma = 5/3$. The plasma fluid is assumed to have infinite electrical conductivity such that flux is conserved to the limits of numerical diffusion. Sun-centered gravitational forces on the plasma are included, and prescribed volumetric heating of the plasma provides the necessary thermal pressure to drive the solar wind. With these assumptions, the system is described by the ideal MHD equations, which are solved in the following conservative form:

$$\frac{\partial \rho}{\partial t} + \nabla \cdot (\rho \mathbf{u}) = 0 \tag{1}$$

$$\frac{\partial (\rho \mathbf{u})}{\partial t} + \nabla \cdot \left[\rho \mathbf{u}\,\mathbf{u} + \left(p + \frac{B^2}{8\pi} \right) I - \frac{\mathbf{B}\,\mathbf{B}}{4\pi} \right] = \rho \mathbf{g} \tag{2}$$

$$\frac{\partial \mathbf{B}}{\partial t} + \nabla \cdot (\mathbf{u}\,\mathbf{B} - \mathbf{B}\,\mathbf{u}) = 0 \tag{3}$$

$$\frac{\partial \varepsilon}{\partial t} + \nabla \cdot \left[\mathbf{u} \left(\varepsilon + p + \frac{B^2}{8\pi} \right) - \frac{(\mathbf{u} \cdot \mathbf{B})\,\mathbf{B}}{4\pi} \right] = \rho \mathbf{g} \cdot \mathbf{u} + (\gamma - 1) Q, \tag{4}$$

where ρ is the plasma mass density, $\mathbf{u}$ the plasma velocity, $\mathbf{B}$ the magnetic field, and p is the plasma pressure (sum of the electron and ion pressures). The volumetric heating term, Q, parameterizes the effects of coronal heating as well as heat conduction and radiation transfer [see *Groth et al.*, 2000]. The gravitational acceleration is defined as $\mathbf{g} = -g(\mathbf{r}/r)(R_s/r)^2$ where R_s is the solar radius and g is the gravitational acceleration at the solar surface. The total energy density, ε, is given by

$$\varepsilon = \frac{\rho u^2}{2} + \frac{p}{\gamma - 1} + \frac{B^2}{8\pi}, \tag{5}$$

where gravity is omitted from the total since it is treated as a momentum source term.

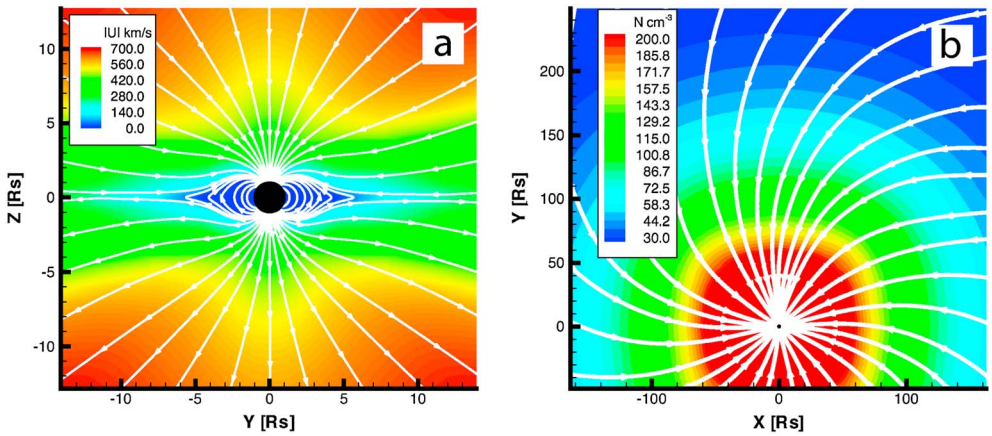

Figure 1. Steady state solar coronal model. (a) A color image of the velocity magnitude of the solar wind solution in the meridional (*y*-*z*) plane with magnetic lines drawn in white. The solar wind shows the fast-slow bimodal distribution associated with solar minimum. (b) The solar wind on the (*x*-*y*) plane located at $z = 25R_s$. Magnetic lines show the Parker spiral while the color image shows the plasma density.

This system of eight equations describes the transport of mass, momentum, and energy coupled to the magnetic field by the induction equation under the assumption of infinite electrical conductivity. These equations are solved in dimensionless form with the block-adaptive tree solar wind Roe-type upwind scheme (BATS-R-US) code [*Powell et al.*, 1999; *Groth et al.*, 2000]. Recently, there have been significant advances in the BATS-R-US solar corona model such that the prescribed volumetric heating has been replaced by physics-based Alfvén wave turbulence [*Sokolov et al.*, 2013; *van der Holst et al.*, 2014].

3. Models of the Steady State Solar Wind and CME

3.1. Steady State Solar Wind Solution

The steady state model of the corona and solar wind described here was developed by *Groth et al.* [2000] and was designed to approximately reproduce conditions near solar minimum. Coronal holes with fast wind are at high latitude, while closed magnetic fields forming a streamer belt are at low latitudes. Slow wind develops at low latitude as a result of flux tube overexpansion. A current sheet forms at the tip of the streamer belt and separates opposite-directed magnetic flux originating from the two poles. Solar rotation is included since the domain extends to more than 300 solar radii at which distance the azimuthal component of the *Parker* [1963] spiral is significant.

The simulation is performed in the inertial frame with the magnetic axis aligned with the *z* axis. The intrinsic magnetic field has dipole and octupole moments aligned with the *z* axis with a maximum field strength of 8.4 Gauss at the poles. The temperature in the model is the plasma total temperature combining electrons and protons, which in general should be taken to be twice that of the actual temperature of either particle species. This total temperature is taken to be 2.85×10^6 K with a plasma density of $\rho = 2.5 \times 10^{-16}$ g cm^{-3} at the base of the corona. Thermal pressure drives the wind outward at supersonic speeds, and in doing so, forms the solar wind [*Parker*, 1963]. Model specifics including parameters that determine the density and temperature of the solar wind and boundary conditions are found in *Manchester et al.* [2006].

Figure 1 provides two-dimensional (2-D) images of the 3-D steady state model with left and right figures showing a meridional plane and the equatorial plane, respectively. Figure 1a shows the velocity magnitude, $|\mathbf{U}|$, of the wind, while the magnetic field is represented by white lines. At high latitude, the magnetic field is carried out with the fast solar wind to achieve an open configuration. Closer to the equator, the slow wind forms with a speed between 300 and 400 km/s. Figure 1b shows a color image of mass density with magnetic lines shown in white in the form of the Parker spiral.

3.2. Gibson-Low Flux Rope

The CME is initiated within this coronal model by superimposing a 3-D Gibson-Low magnetic flux rope [*Gibson and Low*, 1998] in the streamer belt in an initial state of force imbalance as was first described in *Manchester et al.* [2004a, 2004b]. This flux rope is mathematically derived by applying a stretching transformation $r \rightarrow r - a$ to an axisymmetric, spherical ball of twisted magnetic flux and its contained plasma. This

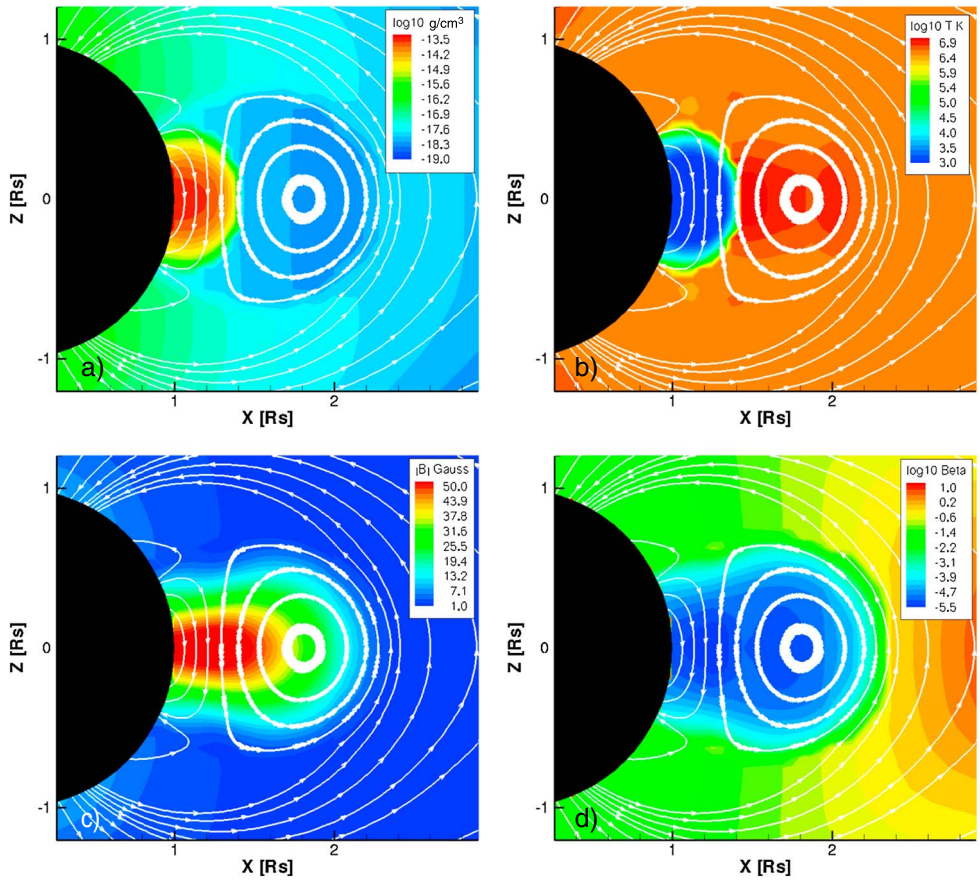

Figure 2. The initial state of the low corona with the imbedded magnetic flux rope shown on the meridional (*x*-*z*) plane. (a) A color image of the $\log_{10}$ of the mass density and (b) the $\log_{10}$ of the plasma temperature. Note the classical three-part plasma structure: a cold dense core of plasma at the base of the flux rope (approximating a filament) contained within a hot low-density cavity in the upper part of the flux rope, which are confined in the coronal streamer. (c) Magnetic field strength in color and (d) the plasma beta. In all panels, magnetic lines are drawn to show the magnetic field confined to the *x*-*z* plane.

mathematical procedure distorts the spherical magnetic flux rope into a tear-drop shape, producing Lorentz forces that require both the pressure and weight of plasma in a $1/r^2$ gravitational field to be in static equilibrium. The density structure of the model possesses a low-density cavity embedded with a dense core at the base of the flux rope that serves to model a filament. For the given field strengths, the corona is unable to provide the required pressure for equilibrium, thus leaving the flux rope in a state of force imbalance that drives the eruption.

The flux rope and contained plasma are linearly superimposed upon the existing corona so that the mass and magnetic field of the flux rope are added directly to the corona. Figure 2 shows the corona containing the Gibson-Low (GL) flux rope. Figures 2a and 2b provide color images of the mass density and temperature, respectively. Here a cold high-density core is found at the base of the flux rope for which the upper extremity is filled with a hot low-density plasma. The core material is roughly 100 times denser and 100 times cooler than the surrounding corona [*Hundhausen*, 1993; *Karpen and Antiochos*, 2008], thus reproducing the thermodynamic properties of a filament. However, it is important to note that this model filament fills a large volume of space and is not highly structured and filamentary as is observed. In total, 2.0×10^{17} grams of dense plasma is added to the corona within the GL flux rope, which is an order of magnitude greater than that observed in filaments. Figure 2c shows a color image of the magnetic field strength, which is approximately 30–50 Gauss. In all panels, the direction of the field is confined to the *x*-*z* plane and is illustrated with white lines.

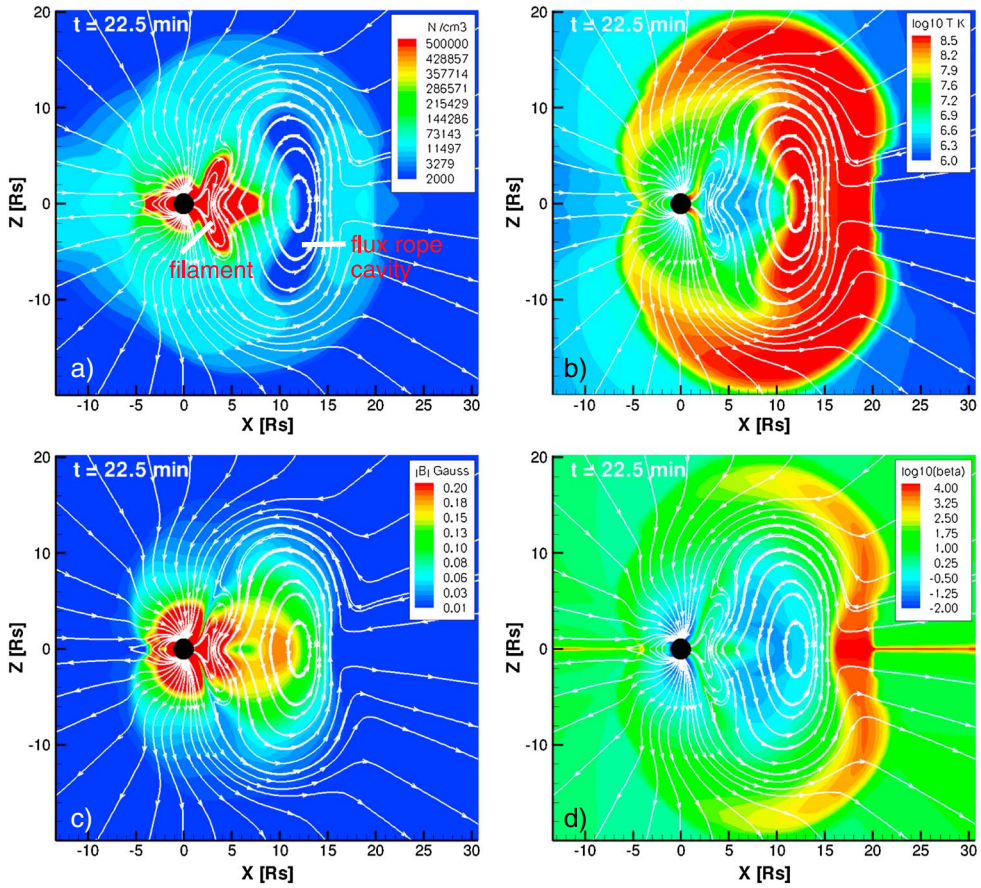

Figure 3. Structure of the CME on the central meridional plane at time 22.5 min after initiation. Panels show the (a) plasma density, (b) temperature, (c) magnetic field strength, and (d) plasma beta. The plasma density shows expanded three-part structure (helmet, cavity, and core) found in the initial state, while the temperature shows significant elevation of the initial state. The field strength/*beta* remains high/*low* compared to the surrounding corona.

4. Examination of CME Simulation

4.1. The CME Morphology and Propagation

In this section, we reexamine the simulation of *Manchester et al.* [2006], which was designed to match the travel time of the Carrington Event of 1859. Upon initiation at $t = 0.0$, the flux rope rapidly accelerates to speeds of approximately 4000 km/s, giving the CME a kinetic energy of 8.0×10^{33} ergs, which again is extreme: an order of magnitude more than that of a typical fast event. The structure of the flux rope close to the Sun (at time $t = 22.5$ min) is shown in Figure 3. Here Figures 3a–3d show the proton density, temperature, magnetic field strength, and plasma beta, which appear in the same order as those shown in Figure 2.

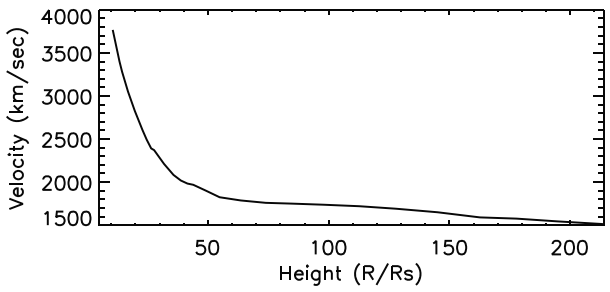

Figure 4. ICME velocity as a function of distance from the Sun. The CME show rapid deceleration near the Sun, then nearly constant speed beyond 50 R_s.

Comparison between the initial state and the CME in Figure 3 reveals nearly self-similar evolution as the features of the flux rope appear in roughly equal proportion. Some exceptions to self-similarity are seen in the filament, which shows poleward expansions. While the filament is still cooler than the surrounding flux rope, its temperature has increased significantly as a result of dissipation of the magnetic energy. The plasma beta has also increased throughout the flux rope.

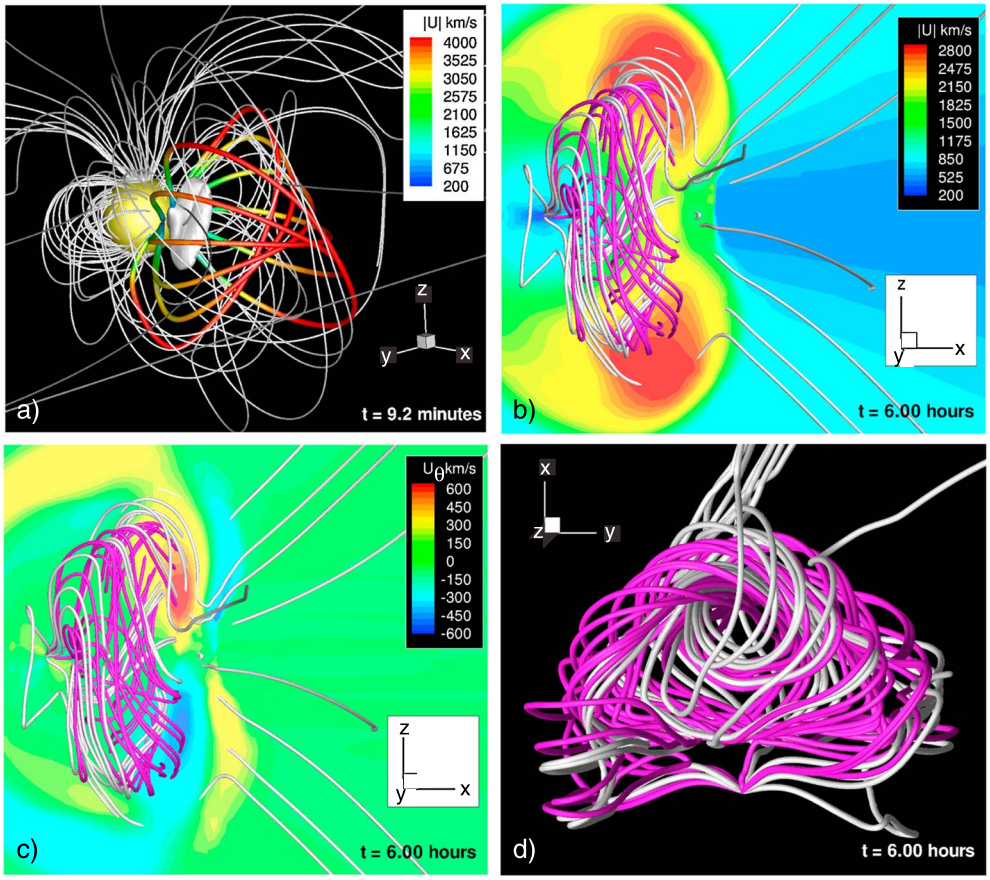

Figure 5. Three-dimensional representations of the ICME magnetic field. (a) The CME at 9.2 min after initiation, with field lines of the flux rope colored to illustrate velocity while the gray isosurface shows the erupting filament. Magnetic field lines outside the flux rope are plotted in white. (b–d) The flux rope at time $t = 6$ h with closed field lines drawn in purple and open field lines (those that have reconnected with open flux of the solar wind) drawn in white. Figures 5b and 5c show the velocity magnitude and latitudinal velocity respectively on the meridional plane, while Figure 5d shows the flux rope seen from the north pole. In all panels, the field lines are the same.

The CME velocity (at the nose of the flux rope) is shown as a function of distance in Figure 4. In the first 50 R_s the CME shows a nearly exponential decay in speed, consistent with the empirical relationship discovered by *Sheeley et al.* [1999] and found in earlier simulations [*Manchester et al.*, 2004a]. Beyond 50 R_s, the speed decreases much more slowly, gradually approaching a speed of 1500 km/s. With deceleration, self-similar evolution in spherical geometry breaks down and the aspect ratio of the flux rope begins to increase drastically (pancaking) as can be seen in Figure 5. Here Figure 5a shows the system 9.2 minutes after initiation where the flux rope field lines are colored to show velocity. Field lines outside of the rope are shaded gray, as is an isosurface of mass density at 1.23×10^{-24} g cm^{-3}, which shows the location of the filament material. Figures 5b–5d show the system from two different perspectives 6 h after initiation. Figures 5b and 5c show the system on the central meridional plane, colored to show the velocity magnitude and the latitudinal flows, respectively. The latitudinal flows show a reversal, first moving toward the equator at the shock (a result of the shock indentation as described in *Manchester et al.* [2005]) and then moving toward the pole in the sheath. Figure 5d shows magnetic field lines from the north solar pole. In all three Figures 5b–5d, closed field lines of the rope are shown in purple, while open field lines are shown in gray. At 6 h, the flux rope is clearly deformed to a prolate shape. Signs of flux rope erosion are seen where field lines at the periphery of the flux rope no longer form closed loops but rather connect to the open flux of the solar wind.

To better understand the evolution of the flux rope, we show its structure on the equatorial plane (x-y) in Figure 6. Here six panels Figures 6a–6f show, respectively, the mass density, temperature, radial velocity,

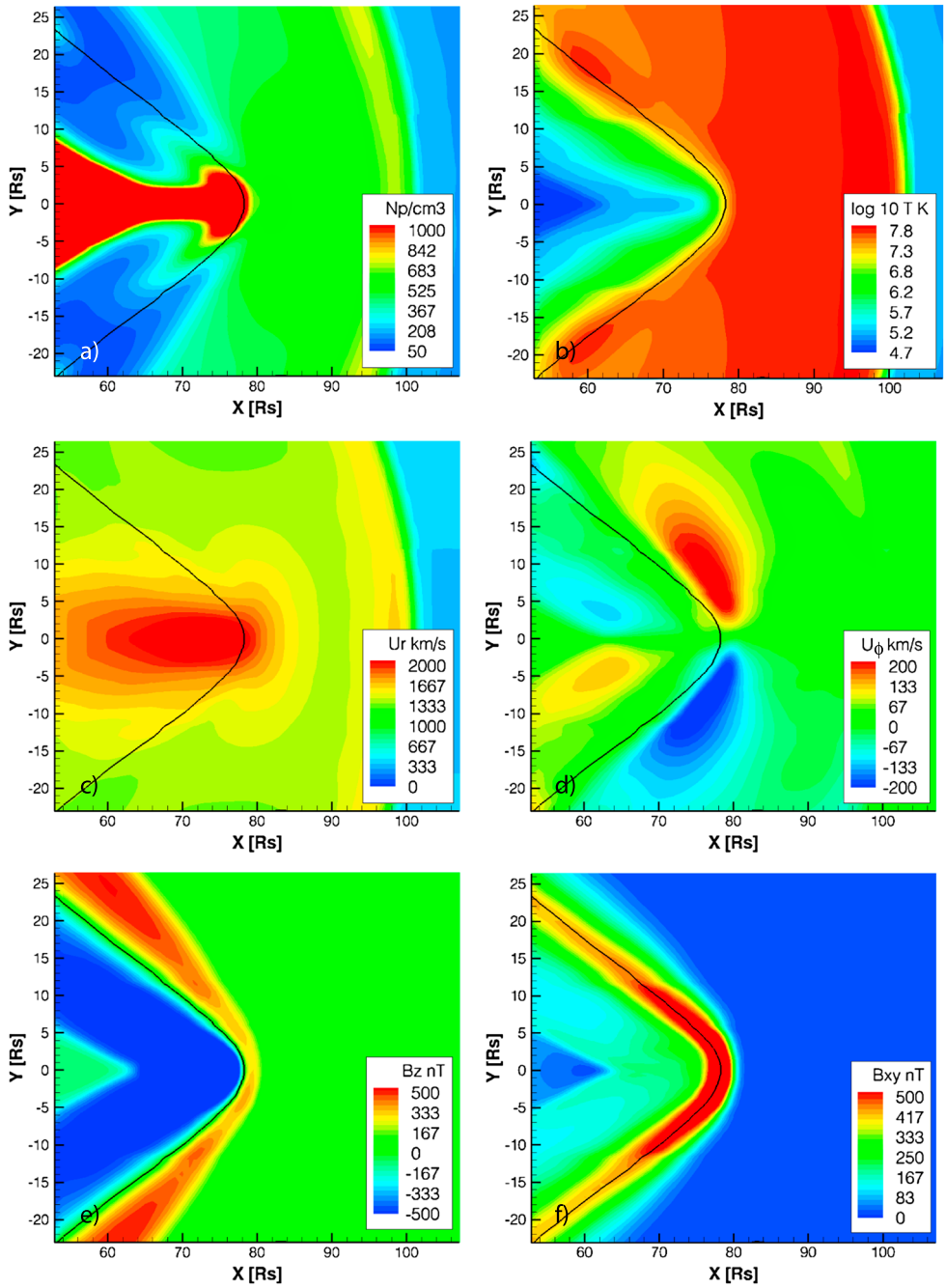

Figure 6. Structure of the ICME seen on the equatorial (*x*-*y*) plane at 6 h. The sequence of panels show the (a) proton density, (b) $\log_{10}$ temperature, (c) radial velocity, (d) azimuthal velocity, (e) B_z, and (f) B_{xy}. The black line is defined by the contour for $B_z = 0$, indicating the axis of the flux rope. Figures 6a and 6b show dense cold material extending forward to the $B_z = 0$ contour. Figure 6c shows the radial velocity peaked at the dense filament material while Figure 6d shows the diverging azimuthal velocity, which transports poloidal flux away from the nose of the ICME thus weakening B_z shown in Figure 6e. On the contrary, compressive radial flows enhance the axial field strength at the nose of the ICME seen in Figure 6f.

azimuthal velocity (in the angular direction about the polar axis), poloidal field (B_z), and the toroidal field strength (axial component, B_{xy}). In each panel, the black line corresponds to the $B_z = 0$ contour, which is the axis of the flux rope. Together, the images illustrate the transport of mass and magnetic flux within the flux rope. Beginning with Figures 6a and 6b, we see cool dense filament material extending to the axis of the flux rope, which is in contrast to the hot plasma in the leading part of the ICME and the sheath. Figure 6c shows

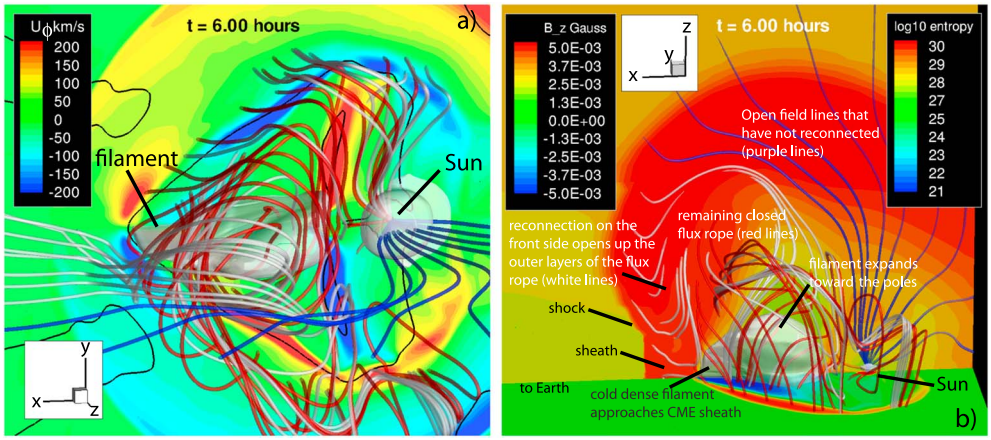

Figure 7. Three-dimensional structure of the ICME seen at 6 h. (a) The azimuthal flow on the equatorial plane with a gray translucent isosurface showing proton density at 4000 cm^{-3}. (b) B_z on the equatorial plane and $\log_{10}$ of the entropy on the meridional plane (x-z) plane. In both panels, magnetic field lines are colored to show their topology: red indicates closed flux rope field lines, white indicates field lines of the flux rope that have reconnected with the open flux of the solar wind, and purple indicates open flux that has not undergone reconnection.

the filament material moving forward through the flux rope with the highest radial velocity in the ICME. The azimuthal velocity shown in Figure 6d exhibits flows diverging from the nose of the ICME outside of the flux rope axis. These flows distort the magnetic flux rope as shown in Figures 6e and 6f. Figure 6e shows that positive B_z flux has been transported away from the nose of the flux rope, leaving only a thin weak layer, while at the same location Figure 6f shows that the toroidal flux has been intensified by the compressive radial flows. Note that the azimuthal flows are effectively blocked by the rope's toroidal field so that the poloidal flux (negative B_z) on the sunward side of the rope remains intact.

To better understand the structure of the ICME as it relates to the flow patterns shown in Figure 6, we examine the flux rope, filament, and flows in fully three dimensions as shown in Figure 7. Here magnetic field lines are colored to illustrate their topology: red lines are those of the flux rope still connected to the Sun on both ends, white lines are those of the flux rope that have reconnected with the interplanetary magnetic field (IMF), and purple lines are those belonging to the open flux of the solar wind. An isosurface of mass density (translucent white) shows the filament material. Figure 7a shows the azimuthal flow on the equatorial plane along with the contour for $B_z = 0$, which shows the axis of the flux rope. Figure 7b shows the magnitude of B_z on the equatorial plane and the plasma entropy on the meridional plane (x-z). Together, these images show the filament material moving to the nose of the flux rope, all the way to its axis as can also be seen in Figure 6a. On the far side of the axis, azimuthal flows carry the poloidal flux away from the nose of the flux rope leaving only a very thin layer of positive B_z. The plot of plasma entropy clearly distinguishes the shocked plasma from the low entropy of the ICME filament material. At the nose of the ICME, we find the filament material is nearly in contact with the shocked plasma of the ICME.

The simulation shows two significant processes affecting the magnetic field of the ICME flux rope: magnetic erosion by reconnection and flux transport by azimuthal flows. Reconnection occurs over a significant area of the rope, both front and rear, while azimuthal flows are found to remove poloidal flux primarily at the nose of the flux rope. To quantify the relative importance of these two effects at the heliospheric equator, we calculate the total unsigned B_z flux on the equatorial plane integrating on a subregion of the domain extending from $-48\,R_s < x < 192\,R_s$ and $-120\,R_s < y < 120\,R_s$, and we plot the flux as a function of time in Figure 8a. We find a large rapid drop in flux during the first hour of the CME when the flux drops 14% from an initial value of 1.4×10^{23} Mx. After this fast drop, there is minor rebound followed by a much slower decay in which the system loses only an additional 7% of B_z flux, which falls to a value of 1.12×10^{23} Mx. This rather modest loss of flux is the result of reconnection between the flux rope and the IMF that opens the poloidal flux, removing it from the equatorial plane. In stark contrast, Figure 8b gives a plot of B_z as a function of radius (along the x axis) 6 h after initiation. This plot shows that the imbalance of B_z at the nose of the flux rope is much greater than would be expected from reconnection alone. While nearly 80% of the original poloidal flux is intact, at the nose of the flux rope there is more than 10 times as much negative flux

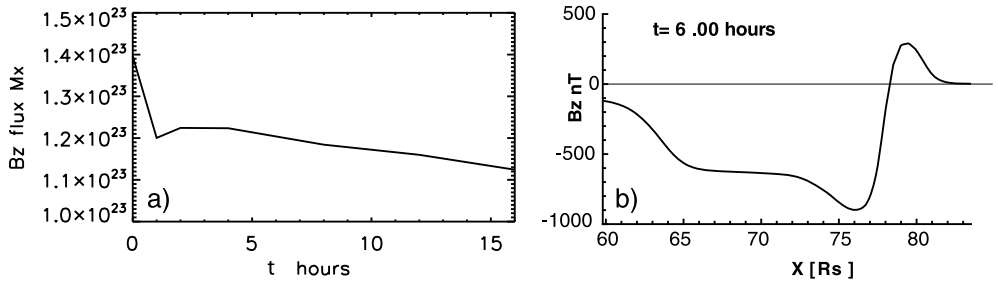

Figure 8. ICME poloidal flux (B_z) as a function of time and space. (a) The total unsigned B_z flux is integrated on the equatorial (x-y) plane and shown as a function of time. The flux rapidly decreases during the first hour after the CME initiation, which is followed by a much lower decay rate as the CME propagates to 1 AU. (b) A line plot of B_z along the x axis at time $t = 6$ h. Note the tremendous asymmetry of the poloidal flux.

as positive. This large imbalance is due to the advection of poloidal flux by strong azimuthal flows driven by the penetration of the dense filament material.

5. Comparison With the 21 January 2005 ICME

The question we now address is whether there are any observed CMEs/ICMEs that share basic features of this simulation, suggesting that the previously unrecognized processes of mass and flux transport shown here are indeed relevant to ICMEs under certain circumstances. We find such a CME in one of the most energetic eruptions of solar cycle 23. On 20 January 2005 just before 07:00 UT, the Sun produced an enormous outburst of energy with near record levels of emission across the electromagnetic and particle spectrum [*Grechnev et al.*, 2008], including an X7.1 class flare, and the second largest ground-level-enhancement (GLE) of cosmic rays ever recorded. This outburst was accompanied by one of the fastest CMEs ever observed, estimated by *Gopalswamy et al.* [2005] to have reached a maximum (plane-of-sky) speed of nearly 3000 km/s. This speed was confirmed by interplanetary scintillation (IPS) measurements [*Pohjollainen et al.*, 2007], which showed the CME decelerated from 2500 km/s at 50 R_s from the Sun to ≈ 1000 km/s at 1 AU. In addition to being very fast, this CME is similar to the simulation in having a three-part structure of cavity, core, and bright loop. At 17:11!UT on the following day, the subsequent ICME arrived at Earth with a speed of 1000 km/s, traveling from the Sun in just 34 h. As will be shown in detail, the ICME shares three unusual features with the simulation: First, the ICME contained a large amount of filament material. Second, this dense plasma was found directly behind the sheath, rather than at the back of the ejecta. Third, the poloidal magnetic field (B_z) within the ICME ejecta was almost entirely of a single polarity.

Observations of the January 21 ICME by the ACE and Wind spacecraft are shown in Figure 9. Figures 9a, 9b, and 9c show the proton speed, density, and temperature, respectively. Figures 9d and 9e show the total magnitude and the z component of the magnetic field, respectively. Figures 9f and 9g show the suprathermal electron pitch angle distribution and the helium$^+$ to helium^{2+} abundance ratio, respectively. Within these plots, there are two obvious discontinuities, the shock and the tangential discontinuity (TD), which separates the ejecta from shocked solar wind plasma. These transitions are marked with (S) and (D), respectively. At the shock, the proton speed increases from 550 km/s to 900 km/s, proton density and temperatures increase by a factor of 4 and 10, respectively, and then remain relatively constant until reaching the TD. This region between the shock and the TD is the sheath, which is numbered 1 at the top of Figure 9a. The CME ejecta and relaxation region are numbered 2 and 3 respectively.

Passing through the TD, we enter the ICME ejecta and encounter the most significant similarity with the simulation. Often the ejecta has the form of a magnetic cloud where the proton density and temperatures decrease and field strengths increase and make a smooth rotation, suggesting the form of a flux rope. However, this event instead follows the pattern shown in the numerical model where the proton density undergoes a large increase at the TD and in the event increases by a factor of 3 to 40 cm^{-3}. At the same time, the temperature drops indicating that the high density is not the result of an adiabatic compression. We note too that the B_z polarity of the ICME ejecta is almost entirely positive. Relating these observations to the model, we come to the conclusion that the flux imbalance is the result of the azimuthal transport of poloidal flux, rather than the result of magnetic reconnection. The presence of counterstreaming electrons

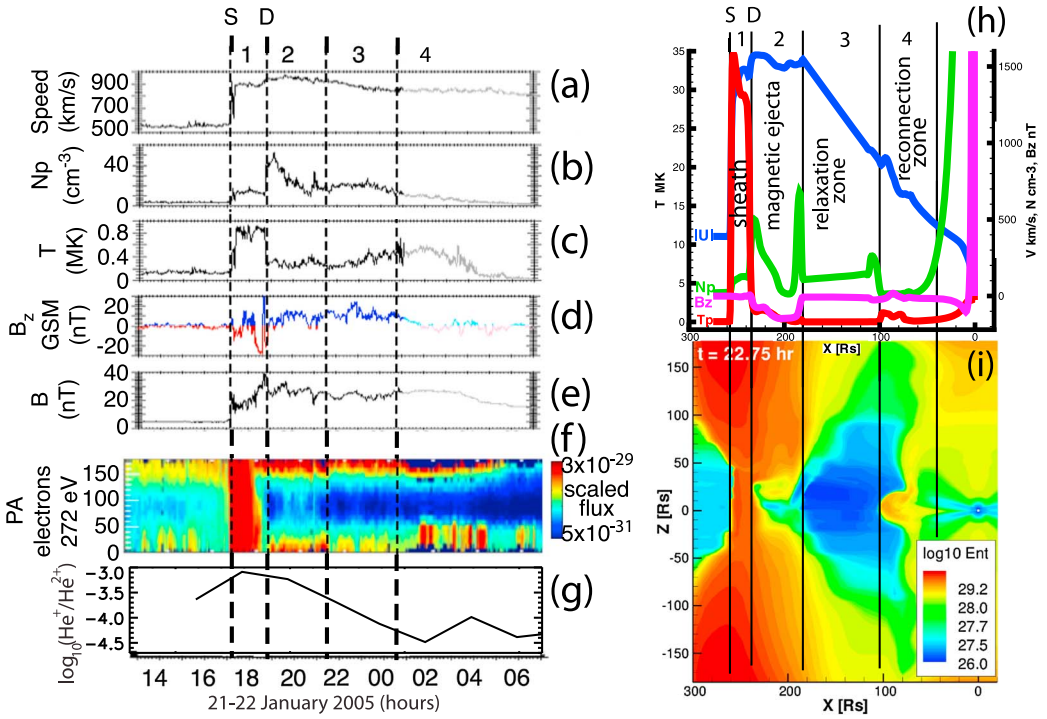

Figure 9. Comparison between the numerical simulation and the 21 January 2005 ICME event. The time evolution of plasma parameters observed at 1 AU are shown on the left-hand side. Here panels show the (a) proton speed, (b) density, (c) temperature, (d) *z* component, (e) the total magnitude of the magnetic field, (f) the suprathermal electron pitch angle distribution, and (g) the He^+ to He^{2+} abundance ratio. (h) Model results with physical quantities plotted as a function of radial distance along the central axis (*x* axis) of the ICME shown for comparison. Here the proton speed (*Up*) and density (*Np*) along with the plasma total temperature and the *z* component of the magnetic field are plotted. (i) A color image of the plasma entropy on the central meridional plane of the model. The density, velocity, temperature, and magnetic field show similarities in basic structure.

in the data suggest that the unipolar flux remains closed rather than being opened to the solar wind by magnetic reconnection.

As previously noted, elevated levels of low-charge-state ions are a strong indicator of filament material in the solar wind. In the 21–22 January 2005 event, we find that the He^+/He^{2+} ratio increases by almost an order of magnitude in passing from the shock to the front of the magnetic ejecta, which suggests that filament material has come in direct contact with the TD. Here the He^+/He^{2+} ratio was determined from ACE/SWICS data by application of triple coincidence criteria for detection, namely, a combination of time-of-flight, energy/charge, and total energy [*Gloeckler et al.*, 1998; *von Steiger et al.*, 2000]. The combination of criteria greatly increase the confidence in the He^+ detection by eliminating the possibility of stray ions polluting the signal. However, the absolute level of He^+ remains somewhat uncertain because the kinetic energy of He^+ in this event lies in close proximity to the instrument detection threshold, implying that some of the signal may be lost. The He^+ levels shown should thus be regarded as a conservative lower minimum to the actual amount present in this event.

The filament material measured by Wind in the 11 February 1997 ICME [*Gopalswamy et al.*, 1998] has characteristics very similar to the filament material identified in the 21 January 2005 ICME. First, in both events, the filament proton density is high and peaks at 40 cm^{-3}. Second, in both events the filament proton temperature is low, which is particularly true of the 1997 event where the proton thermal velocity of only 20 km/s (16,000 K). Third, in both cases the filament material has elevated levels of low-charge state ions. The main difference between these two events is that the 1997 event is of moderate speed. When the front of the CME (at 25 R_s) is moving at 750 km/s, the filament material is moving at only 390 km/s. At this same time, the front of the CME is still accelerating at ≈ 17 m s^{-2}, while the filament material accelerates at only ≈ 4 m s^{-2}, so it is destined to remain at the back of the magnetic cloud where it was found by Wind instruments. This

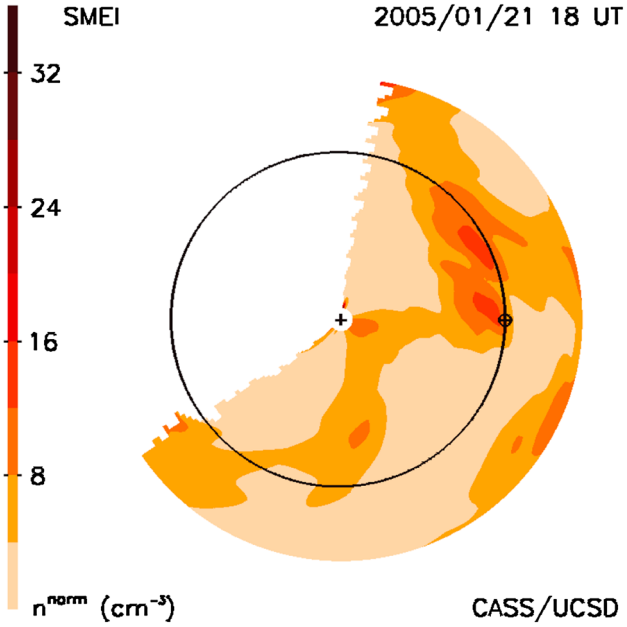

Figure 10. Three-dimensional reconstruction of the solar wind density during 21 January 2005 ICME. Reconstructions are made with SMEI observations and show proton density normalized to remove the r^{-2} fall off. The position of the Earth is marked with cross-in-circle and the Sun is located at the center of the image. White areas are where no reconstruction was possible. Note the region of high density impacting Earth consistent with the in situ data. This ecliptic-cut figure from the 3-D reconstructions is provided by the University of California, San Diego (UCSD) SMEI research team led by B. Jackson.

movement is in contrast to the strong deceleration experienced by very fast CMEs such as the 20 January 2005 CME, which may drive dense filament material to the front of the ICME.

For a more detailed comparison, we reexamine the structure of the model ICME now at 1 AU as shown in the right-hand side of the Figure 9. Here Figure 9h shows plasma properties plotted as a function of distance along the *x* axis with the proton speed, density, and temperature shown in blue, green, and red, respectively, and the *z* component of the magnetic field is plotted in purple. The same three regions of the observed ICME, the sheath, ejecta, and the relaxation zone are numbered 1, 2, and 3, respectively. A fourth region, the reconnection zone is numbered 4. Figure 9i provides a color plot of the plasma entropy on the meridional plane. Examining the plots in Figure 9h, we first note the presence of a stronger shock where the velocity increases from 370 km/s to 1350 km/s. In the sheath, the temperature, density, and magnetic field strength remain nearly constant, and the velocity only increases moderately, similar to the observed event. At $r = 260\,R_s$, we encounter the TD marking the boundary between the sheath and the ICME ejecta. Here we enter the filament material where the temperature drops, the density increases by a factor of five, and the magnetic field strength increases abruptly as B_z approaches a value of −200 nT, remaining unipolar in B_z through the ejecta.

The model ICME resembles several distinct features of the ICME observed on 21 January, yet there is an important distinction that needs to be examined. The effacing of poloidal flux $(+B_z)$ and filament material in contact with the sheath are found only at the nose of the ICME, while the 20 January CME occurred far from disk center, implying that only the flank of the ICME encountered the Earth. So how then could the basic transport processes found in the model apply? A possible answer may be found in the tomographic 3-D reconstructions of plasma density for the 21 January ICME made with data from the Solar Mass Ejection Imager (SMEI) as shown in Figure 10 [*Jackson et al.*, 2010]. Here we see color contours showing the proton density on the ecliptic plane at time 18 UT on 21 January. The density is normalized to 1 AU to remove the r^{-2} fall off, and the location of the Earth on its orbit is marked with a small circle containing a cross. The density structure shows a discontinuous front with two regions of enhancement, with the margin of one seen impacting the Earth. While the CME was far from disk center, it produced a dense localized disturbance that impacted the Earth, which in situ observations show to be highest in density immediately behind the sheath. Thus, the structure has a localized region of high density impacting the Earth that may be consistent with the numerical model.

6. Summary and Conclusions

The CME model we examined possesses the common characteristics of the three-part preevent density structure, including a dense helmet streamer threaded by a magnetic flux, which contains a low-density cavity and a high-density core at the base of the rope approximating a coronal filament. The flux rope and the three-part density structure are expelled from the corona as a high speed CME, which initially evolves in

a self-similar fashion. As the ICME propagates through the solar wind, it undergoes strong deceleration such that the denser filament material moves to the front of the ICME and comes in direct contact with the sheath material. Strong azimuthal flows develop in front of the protruding filament material and transport poloidal flux away from the nose of the ICME producing a large imbalance in B_z, giving the appearance of flux rope erosion by magnetic reconnection while in fact the majority of the flux remains intact.

When compared with the CME that erupted from the Sun on 20 January 2005 and passed the Earth the following day, we find several significant similarities. First, the 20 January CME was a very fast CME with a high initial speed of $\approx$ 3000 km/s that underwent strong deceleration and arrived at Earth traveling nearly 1000 km/s. Very dense plasma was found at the CME front, adjacent to the sheath, where one would usually expect to find a low-density cloud. The low temperature of the plasma indicates that the density enhancement was not the result of an adiabatic compression, and the helium charge state abundances suggest that the dense plasma is indeed filament material. In this region of the CME ejecta, we find a large imbalance in poloidal flux (B_z), which in other events has been characterized as flux rope erosion due to reconnection between the rope magnetic field and the IMF [*Dasso et al.*, 2006; *Ruffenach et al.*, 2012; *Lavraud et al.*, 2014]. The simulation suggests an alternative mechanism, namely, that this flux imbalance may be partially due to the transport of poloidal flux by azimuthal flows. Such flows may occur when dense material decelerates more slowly than the surrounding ICME such that it begins to protrude forward and comes in contact with the sheath. More evidence in support of this mechanism being at work in the 21 January 2005 ICME is found in the counterstreaming suprathermal electrons, which indicate that the imbalanced magnetic flux is still in a closed configuration and has not yet reconnected with the IMF, just as is found in the model.

In making our comparison with the model, we have interpreted the 21 January data to represent a distorted flux rope for which the axis passes close to the ecliptic and points largely in the longitudinal direction. There are, however, different interpretations of the structure of this ICME. *Foullon et al.* [2007] concluded that the axis of the rope was located west of the Earth and that it was oriented nearly perpendicular to the ecliptic. *Rodriguez et al.* [2008] came to yet a different interpretation. They proposed that ACE passed through the leg of the flux rope lying near the ecliptic where the axis was close to the Earth-Sun direction, a notion supported by the origination of the CME from the western limb. While these are both valid interpretations of the 21 January ICME, our interpretation is in line with that of *Dasso et al.* [2006] who argued that the flux rope axis was located near the equatorial plane and that the B_z flux imbalance was due to erosion. Although we propose a different erosion mechanism, namely, sideways flux transport stemming from the protrusion of dense material, it remains that in either case the extreme erosion transforms an originally S-N magnetic cloud into a structure for which almost only the northward B_z portion remains. Such a strong alteration of the magnetic structure of the magnetic cloud means that the classical method used (minimum variance analysis (MVA) or flux rope fitting) will be strongly biased, if not simply irrelevant, to determine the actual axis orientation of the initial flux rope. Such was also illustrated in *Owens et al.* [2012] in the different, yet consistent, context of the impact of various crossing trajectories on the outputs of such methods. We thus argue that the axis of the magnetic cloud under study could initially well be pointing in the ecliptic, but that the application of classic methods after erosion will alter this determination.

In addition, we need to qualify our interpretation of the filament material. Coronal mass ejections have been shown to often exhibit bimodal charge state distribution in heavy ions, with peaks at slow solar wind values along with contributions from hotter flare-related plasma or cooler filament-related plasma simultaneously observed [*Gruesbeck et al.*, 2011]. In this case, the cool contributions are shown by the abundance of He^+, which becomes measurable due to the enhancement in density related to the filament material [*Lepri and Zurbuchen*, 2010]. The lack of signatures in the heavier ions in this event is likely due to the filament material possibly being too cold to be detected by typical analysis methods (e.g., singly charged C^+, O^+, or lower than Fe^{4+}) or being too low density to be detected. To address this point by way of numerical simulation requires a complete treatment of the thermodynamics of the plasma along with a time-dependent plasma charge state calculation. Such advanced simulations are just beginning to be made [*Lynch et al.*, 2011; *Jin et al.*, 2012].

The model possesses a number of limitations that should be mentioned. First, the model corona is representative of solar minimum while it is known that January 2005 was during the deep declining phase of the solar cycle with several large active regions present, which would result in a more structured solar wind than the model possesses. Second, the plasma's mass density at 1 AU is too high by a factor of 3, which must be

offset by the mass and momentum of the CME to achieve the high speed and short transit time. The amount of filament plasma contained within the flux rope is closely linked to the magnetic field strength of the rope, which also determines the speed of the ejecta. In this case, high speed is accompanied by a filament mass that is more than the mass typically observed in CMEs. The model is both idealized and extreme in mass and energy, which cannot match the specific details of the 20 January 2005 CME, but it illustrates basic mass and flux transport processes that may occur to a lesser degree when a fast ICME with concentrated material undergoes strong deceleration in the solar wind. Most importantly, the simulation illustrates that flux imbalances characterized as flux rope erosion in ICMEs may be partially due to transport of poloidal flux by azimuthal flows.

Understanding the processes that transport extremes in solar wind density and pressure to the Earth is important because some of the largest and most damaging space weather events ever observed contained similar intervals of dense solar material. The similarities in the ICMEs that triggered the January 2005 event and the Carrington 1859 magnetic storm [*Manchester et al.*, 2006; *Li et al.*, 2006], offer intriguing evidence that a solar filament may have played a role in the largest storm in recorded history [cf., *Tsurutani et al.*, 2003]. Unusually dense solar wind was also observed just behind the sheath during the 4–5 August 1972 event [*Vaisberg and Zastenker*, 1976; *DÚston et al.*, 1977], caused by one of the fastest CMEs ever observed [*Cliver et al.*, 1990], which disrupted a major communications system in the United States [*Boteler and van Beek*, 1999]. Recently, solar filament material has been identified in ICMEs that produced the 3–5 August 2010 storm and the 20 November 2003 superstorm [*Sharma et al.*, 2013]. The 3–5 August 2010 geomagnetic storm was driven by a massive solar filament eruption on 1 August 2010 involving the entire Earth-facing hemisphere of the Sun [*Schrijver and Title*, 2011].

The analysis in *Kozyra et al.* [2014], the companion to this paper, demonstrates the potential for a significant solar filament collision to amplify the effects of an ICME on the Earth's space environment through the rapid formation of a massive cold dense plasma sheets (CDPS) in a compressed magnetosphere. But the implications are far-reaching. If the IMF had rotated southward after the formation of the CDPS, the dense material would have been transported earthward providing the source population for an extreme ring current [cf., *Thomsen et al.*, 2003] and possibly triggering a superstorm. Other processes that increase the geoeffectiveness of an ICME in the presence of dense solar material are possible.

Both the reconnection rate at the leading edge [cf., *Taubenschuss et al.*, 2010] and the momentum of the filament material increase with the speed of the ICME. The present work implies that the extent of the redistribution of the filament material within the ICME and the flux rope erosion should both be a function of its speed, adding new information to address why significant solar filament material makes it to Earth in cases like the 21 January 2005 event and not others. Though rare, the understanding and prediction of these extreme events are of intense interest because disastrous economic and societal impacts (most notably the loss of services from Earth-orbiting satellites, and the disruption of power grids on a global scale) are anticipated should a 100 year storm occur in modern times.

Acknowledgments

W. Manchester was supported by NASA grants NNX13AG25G, NNX11AO60G, and NSF grant AGS 1322543, and J. Kozyra was supported by NASA grants NNX10AQ34G, NNX11AO60G, and NSF grant ATM 0903596. The simulation data presented in this paper are available on the web at http://herot.engin.umich.edu/~chipm/files/Carrington/.

Yuming Wang thanks Pascal Demoulin and an anonymous reviewer for their assistance in evaluating this paper.

References

Basu, S., K. M. Groves, H. C. Yeh, S.-Y. Su, F. J. Rich, P. J. Sultan, and M. J. Keskinen (2001), Response of the equatorial ionosphere in the South Atlantic region to the great magnetic storm of July 15, 2000, *Geophys. Res. Lett.*, *28*(18), 3577–3580.

Boteler, D. H., and G. J. van Beek (1999), August 4, 1972 revisited: A new look at the geomagnetic disturbance that caused the L4 cable system outage, *Geophys. Res. Lett.*, *26*(5), 577–580.

Burlaga, L. F., E. Sittler, F. Mariani, and R. Schwenn (1981), Magnetic loop behind an interplanetary shock: Voyager, Helios, and IMP 8 observations, *J. Geophys. Res.*, *86*(A8), 6673–6684, doi:10.1029/JA86iA08p06673.

Burlaga, L. F., and K. W. Behannon (1982), Magnetic clouds: Voyager observations between 2 and 4 AU, *Sol. Phys.*, *81*, 181–192.

Burlaga, L. F., K. W. Behannon, and L. Klein (1987), Compound streams, magnetic clouds and major geomagnetic storms, *J. Geophys. Res.*, *92*(A6), 5725–5734, doi:10.1029/JA092iA06p05725.

Burlaga, L. F., et al. (1998), A magnetic cloud containing prominence material: January 1997, *J. Geophys. Res.*, *103*(A1), 277–285.

Cliver, E. W., J. Feynman, and H. B. Garrett (1990), An estimate of the maximum speed of the solar wind, 1938–1989, *J. Geophys. Res.*, *95*(A10), 17,103–17,112.

Dasso, S., C. H. Mandrini, P. Démoulin, and M. L. Luoni (2006), A new model-independent method to compute magnetic helicity in magnetic clouds, *Astron. Astrophys.*, *455*, 349–359.

Démoulin, P. (2008), A review of the quantitative links between CMEs and magnetic clouds, *Ann. Geophys.*, *26*, 3113–3125.

DÚston, C., J. M. Bosqued, F. Cambou, V. V. Temnyi, G. N. Zastenker, O. L. Vaisberg, and E. G. Eroshenko (1977), Energetic properties of interplanetary plasma at the Earth's orbit following the August 4, 1972 flare, *Sol. Phys.*, *51*, 217–229.

Foullon, C., C. J. Owen, S. Dasso, L. M. Green, I. Dandouras, H. A. Elliott, A. N. Fazakerley, Y. V. Bogdanova, and N. U. Crooker (2007), Multi-spacecraft study of the 21 January 2005 ICME evidence of current sheet substructure near the periphery of a strongly expanding, fast magnetic cloud, *Sol. Phys.*, *244*, 139–165.

Gibson, S., and B. C. Low (1998), A time-dependent three-dimensional magnetohydrodynamic model of the coronal mass ejection, *Astrophys. J.*, *493*, 460–473.
Gloeckler, G., et al. (1998), Investigation of the composition of solar and interstellar matter using solar wind and pickup ion measurements with SWICS and SWIMS on the ACE spacecraft, *Space Sci. Rev.*, *86*, 497–539.
Gopalswamy, N., et al. (1998), On the relationship between coronal mass ejections and magnetic clouds, *Geophys. Res. Lett.*, *25*, 2485–2488.
Gopalswamy, N., H. Xie, S. Yashiro, and I. Usoskin (2005), Coronal mass ejections and ground level enhancements, in *Proceedings of the 29th International Cosmic Ray Conference, August 3-10, 2005, Pune, India*, vol. 1, edited by B. Sripathi Acharya et al., Tata Institute of Fundamental Research, Mumbai.
Grechnev, V. V., et al. (2008), An extreme solar event of 20 January 2005: Properties of the flare and the origin of energetic particles, *Sol. Phys.*, *252*, 149–177.
Groth, C. P. T., D. L. DeZeeuw, T. I. Gombosi, and K. G. Powell (2000), Global three-dimensional MHD simulation of a space weather event: CME formation, interplanetary propagation, and interaction with the magnetosphere, *J. Geophys. Res.*, *105*, 25,053–25,078.
Gruesbeck, J. R., S. T. Lepri, T. H. Zurbuchen, and S. K. Antiochos (2011), Constraints on coronal mass ejection evolution from in situ observations of ionic charge states, *Astrophys. J.*, *730*, 103–111.
Hundhausen, A. J., H. E. Gilbert, and S. J. Bame (1968), Ionization state of the interplanetary plasma, *J. Geophys. Res.*, *73*, 5485–5493.
Hundhausen, A. J. (1993), Sizes and locations of coronal mass ejections: SMM observations from 1980 and 1094–1989, *J. Geophys Res.*, *98*, 13,177–13,200.
Jackson, B. V., P. P. Hick, A. Buffington, M. M. Bisi, J. M. Clover, M. S. Hamilton, M. Tokumaru, and K. Fujiki (2010), 3D reconstruction of density enhancements behind interplanetary shocks from solar mass ejection imager white-light observations, in *AIP Conf. Proc., CP1216, Twelfth International Solar Wind Conference*, edited by M. Maksimovic et al., American Institute of Physics, College Park, Md.
Jin, M., et al. (2012), A global two-temperature corona and inner heliosphere model: A comprehensive validation study, *Astrophys. J.*, *745*, 6, doi:10.1088/0004-637X/745/1/6.
Jones, R. A., A. R. Breen, R. A. Fallows, A. Canals, M. M. Bisi, and G. Lawrence (2007), Interaction between coronal mass ejections and the solar wind, *J. Geophys. Res.*, *112*, A08107, doi:10.1029/2006JA011875.
Karpen, J. T., and S. K. Antiochos (2008), Condensation formation by impulsive heating in prominences, *Astrophys. J.*, *676*, 658–671.
Ko, Y., G. Gloeckler, C. M. S. Cohen, and A. B. Galvin (1999), Solar wind ionic charge states during the Ulysses pole-to-pole pass, *J. Geophys. Res.*, *104*, 17,005–17,019.
Kozyra, J. U., W. B. Manchester IV, C. P. Escoubet, S. T. Lepri, M. W. Liemohn, W. D. Gonzalez, M. W. Thomsen, and B. T. Tsurutani (2013), Earth's collision with a solar filament on 21 January 2005: Overview, *J. Geophys. Res. Space Physics*, *118*, 5967–5978, doi:10.1002/jgra.50567.
Kozyra, J. U., et al. (2014), The Earth's interaction with a solar filament on 21 January 2005: Geospace consequences, *J. Geophys. Res. Space Phys.*, doi:10.1002/2013JA019748, in press.
Lavraud, B., A. Ruffenach, A. P. Rouillard, P. Kajdic, W. B. Manchester, and N. Lugaz (2014), Geo-effectiveness and radial dependence of magnetic cloud erosion by magnetic reconnection, *J. Geophys. Res. Space Physics*, *119*, 26–35, doi:10.1002/2013JA019154.
Lee, J.-Y., and J. C. Raymond (2012), Low ionization state plasma in coronal mass ejections, *Astrophys. J.*, *758*, 116, doi:10.1088/0004-637X/758/2/116.
Lepri, S. T., and T. H. Zurbuchen (2010), Direct observational evidence of filament material within interplanetary coronal mass ejections, *Astrophys. J.*, *723*, L22–L27.
Li, X., M. Temerin, B. T. Tsurutani, and S. Alex (2006), Modeling of 1–2 September 1859 super magnetic storm, *Adv. Space Res.*, *38*, 273–279.
Low, B. C. (2001), Coronal mass ejections, magnetic flux ropes, and solar magnetism, *J. Geophys. Res.*, *106*, 25,141–25,163.
Lynch, B. J., A. A. Reinard, T. Mulligan, K. K. Reeves, C. E. Rakowski, J. C. Allred, Y. Li, J. M. Laming, P. J. MacNeice, and J. A. Linker (2011), Ionic composition structure of coronal mass ejections in axisymmetric magnetohydrodynamic models, *Astrophys. J.*, *740*, 112, doi:10.1088/0004-637X/740/2/112.
Lugaz, N., W. B. Manchester IV, and T. I. Gombosi (2005), The evolution of coronal mass ejection density structures, *Astrophys. J.*, *627*, 1019–1030, doi:10.1086/430465.
Manchester, W. B., IV, T. I. Gombsi, I. I. Roussev, D. L. DeZeeuw, I. V. Sokolov, K. G. Powell, G. Tóth, and M. Opher (2004a), Three-dimensional MHD simulation of a flux rope driven CME, *J. Geophys. Res.*, *109*, A01102, doi:10.1029/2002JA009672.
Manchester, W. B., IV, T. I. Gombsi, I. I. Roussev, A. J. Ridley, D. L. DeZeeuw, I. V. Sokolov, K. G. Powell, and G. Tóth (2004b), Modeling a space weather event from the Sun to the Earth: CME generation and propagation, *J. Geophys. Res.*, *109*, A02107, doi:10.1029/2003JA010150.
Manchester, W., IV, T. I. Gombosi, D. L. DeZeeuw, I. V. Sokolov, I. I. Roussev, K. G. Powell, G. Tóth, and T. H. Zurbuchen (2005), CME shock and sheath structures relevant to particle acceleration, *Astrophys. J.*, *622*, 1225–1239, doi:10.1086/427768.
Manchester, W., IV, A. J. Ridley, T. I. Gombosi, and D. L. DeZeeuw (2006), Modeling the Sun-to-Earth propagation of a very fast CME, *Adv. Space Res.*, *38*, 253–262.
Owens, M., P. Demoulin, N. P. Savani, B. Lavraud, and A. Ruffenach (2012), Implications of non-cylindrical flux ropes for magnetic cloud reconstruction techniques and the interpretation of double flux rope events, *Sol. Phys.*, *278*, 435–446.
Parker, E. N. (1963), *Interplanetary Dynamical Processes*, Wiley-Interscience, New York.
Pohjollainen, S., L. van Driel-Gesztelyi, J. L. Culhane, P. K. Manoharan, and H. A. Elliott (2007), CME propagation characteristics from radio observations, *Sol. Phys.*, *244*, 167–188.
Powell, K. G., P. L. Roe, T. J. Linde, T. I. Gombosi, and D. L. De Zeeuw (1999), A solution-adaptive upwind scheme for ideal magnetohydrodynamics, *J. Comput. Phys.*, *154*, 284–309.
Ridley, A. J., D. L. DeZeeuw, W. B. Manchester IV, and K. C. Hansen (2006), The magnetospheric and ionospheric response to a very strong interplanetary shock and coronal mass ejection, *Adv. Space Res.*, *38*, 263–272.
Riley, P., et al. (2004), Fitting flux ropes to a global MHD solution: A comparison of techniques, *J. Atmos. Sol. Terr. Phys.*, *66*, 1321–1331.
Rodriguez, L., A. N. Zhukov, D. Odstrcil, V. J. Pizzo, and D. F. Webb (2008), Evidence of posteruption reconnection associated with coronal mass ejections in the solar wind, *Astrophys. J.*, *578*, 972–978.
Ruffenach, A., et al. (2012), Multispacecraft observation of magnetic cloud erosion by magnetic reconnection during propagation, *J. Geophys. Res.*, *117*, A09101, doi:10.1029/2012JA017624.
Schwenn, R., H. Rosenbauer, and K. H. Muhlhauser (1980), Singly ionized helium in the driver gas of an interplanetary shock wave, *Geophys. Res. Lett.*, *7*(3), 201–204.
Sharma, R., and N. Srivastava (2012), Presence of solar filament plasma detected in interplanetary coronal mass ejections by in situ spacecraft, *J. Space Weather Space Clim.*, *2*, A10, doi:10.1051/swsc/2012010.

Sharma, R., N. Srivastava, D. Chakrabarty, C. Möstl, and Q. Hu (2013), Interplanetary and geomagnetic consequences of 5 January 2005 CMEs associated with eruptive filaments, *J. Geophys. Res. Space Physics*, *118*, 3954–3967, doi:10.1002/jgra.50362.

Skoug, R. M., et al. (1999), A prolonged He+ enhancement within a coronal mass ejection in the solar wind, *Geophys. Res. Lett.*, *26*(2), 161–164, doi:10.1029/1998GL900207.

Sokolov, I. V., B. van der Holst, R. Oran, C. Downs, I. I. Roussev, M. Jin, W. B. Manchester IV, R. M. Evans, and T. I. Gombosi (2013), Magnetohydrodynamic waves and coronal heating: unifying empirical and MHD turbulence models, *Astrophys. J.*, *764*, 23, doi:10.1088/0004-637X/764/1/23.

Schrijver, C. J., and A. M. Title (2011), Long-range magnetic couplings between solar flares and coronal mass ejections observed by SDO and STEREO, *J. Geophys. Res.*, *116*, A04108, doi:10.1029/2010JA016224.

Sheeley, N. R., J. H. Walters, Y.-M. Wang, and R. A. Howard (1999), Continuous tracking of coronal outflows: Two kinds of coronal mass ejections, *J. Geophys Res.*, *104*, 24,739–24,767.

Taubenschuss, U., N. V. Erkaev, H. K. Biernat, C. J. Farrugia, C. MoANstl, and U. V. Amerstorfer (2010), The role of magnetic handedness in magnetic cloud propagation, *Ann. Geophys.*, *28*(5), 1075–1100, doi:10.5194/angeo-28-1075-2010.

Thomsen, M. F., J. E. Borovsky, R. M. Skoug, and C. W. Smith (2003), Delivery of cold, dense plasma sheet material into the near-Earth region, *J. Geophys. Res.*, *108*(A4), 1151, doi:10.1029/2002JA009544.

Tsurutani, B. T., W. D. Gonzalez, G. S. Lakhina, and S. Alex (2003), The extreme magnetic storm of 1–2 September 1859, *J. Geophys. Res.*, *108*(A7), 1268, doi:10.1029/2002JA009504.

Tsurutani, B., et al. (2004), Global dayside ionospheric uplift and enhancement associated with interplanetary electric fields, *J. Geophys. Res.*, *109*, A08302, doi:10.1029/2003JA010342.

Vaisberg, O. L., and G. N. Zastenker (1976), Solar wind and magnetosheath observations at Earth during August 1972, *Space Sci. Rev.*, *19*, 687–702.

van der Holst, B., I. V. Sokolov, X. Meng, M. Jin, W. B. Manchester IV, G. Tóth, and T. I. Gombosi (2014), Alfvén Wave Solar Model (AWSoM): Coronal heating, *Astrophys. J. Supp.*, *782*, 81, doi:10.1088/0004-637X/782/2/81.

von Steiger, R., et al. (2000), Composition of quasi-stationary solar wind flows from Ulysses/Solar Wind Ion Composition Spectrometer, *J. Geophys. Res.*, *105*, 27,217–27,238.

Yao, S., E. Marsch, C.-Y. Tu, and R. Schwenn (2010), Identification of prominence ejecta by the proton distribution function and magnetic fine structure in interplanetary coronal mass ejections in the inner heliosphere, *J. Geophys. Res.*, *115*, A05103, doi:10.1029/2009JA014914.

Zhang, J.-C., M. W. Liemohn, M. F. Thomsen, J. U. Kozyra, M. H. Denton, and J. E. Borovsky (2006), A statistical comparison of hot-ion properties at geosynchronous orbit during intense and moderate geomagnetic storms at solar maximum and minimum, *J. Geophys. Res.*, *111*, A07206, doi:10.1029/2005JA011559.